Wiley
Shock and Vibration
Volume 2025, Article ID 5575921, 14 pages
https://doi.org/10.1155/vib/5575921

Research Article

Optimization Design and Analysis for the Mechanical Test Platform of Scientific Probe Module of the Cool Planet Imaging Coronagraph

Lingyi Kong, Jiangpei Dou, Wei Guo, Mingming Xu, Shu Jiang, and Bo Chen

Solar and Space Instrument Research Laboratory, Nanjing Institute of Astronomical Optics & Technology, Chinese Academy of Sciences, Nanjing, Jiangsu, China

Correspondence should be addressed to Mingming Xu; mingxu@niaot.ac.cn

Received 5 February 2025; Revised 16 July 2025; Accepted 11 August 2025

Academic Editor: Arnab Biswas

This paper optimizes the design and analysis of the mechanical test platform for the scientific probe module of the Cool Planet Imaging Coronagraph, which is the fifth part of the China Space Station survey Telescope. First, according to the module layout and economic requirements, the preliminary structural design of the module mechanical test platform is carried out, and the stiffness sensitive parameters of the assembly are identified to determine the optimization parameters. The central composite design method is used to design the test platform, and a third-order regression model is constructed for response surface analysis. The third-order response surface model of the fundamental frequency and amplitude of the test platform is obtained by fitting the test data with the least squares method, and the structure of the module mechanical test platform is determined. The modal analysis is carried out to determine the fundamental frequency and vibration modes of the mechanical test platform. The vibration response of the platform is simulated by sine, random, and swept frequency vibration simulations. The response surface fitting algorithm is verified by the test platform swept frequency test. The agreement between the response surface fitting algorithm and the experiment is good. The fundamental frequency of the test platform is 436.2 Hz (> 300 Hz), which meets the design index requirements of the test platform and can accurately guide the optimization design work. At the same time, it provides the theoretical basis and design method for the structural design of the Chinese manned space station.

Keywords: China Space Station survey Telescope; Cool Planet Imaging Coronagraph; mechanical test platform; scientific probe module; third-order response surface model

1. Introduction

The China Space Station survey Telescope (CSST) is the first large-scale space survey telescope independently developed by China. It will carry out cutting-edge scientific research in the formation and evolution of cosmic structure, dark matter and dark energy, exoplanets, and solar system bodies. Among them, the Cool Planet Imaging Coronagraph (CPI-C) is one of the important observation equipment of CSST. It is responsible for the high-contrast imaging detection of exoplanets, which has very important scientific significance for my country's independent exploration of exoplanets and the search for the "second Earth" [1].

The CPI-C is divided into a scientific probe module and an integrated power distribution module. The scientific probe module is the optical imaging module in the CPI-C. It integrates an internal occultation optical path system. By adjusting the internal occultation structure, it can block or eliminate starlight and capture and detect planetary light. It is a key technology for confirming terrestrial planets, but it also faces unprecedented challenges. The contrast between a planet and its host star is very different. The target imaging contrast of the scientific probe module needs to reach 10–8 to achieve high-contrast direct imaging research on exoplanets [2–6]. The scientific probe module integrates sensitive optical components such as the internal optical path system and visible light imaging cameras and wavefront cameras. As an important optical system module, the overall rigidity, strength, and structural stability of the module are the basis for achieving the functional performance of the module. As a space optical payload, the scientific probe module must meet the strict mechanical environment requirements of CSST during design to ensure the structural stability and safety of the module under the dynamic environment conditions during rocket launch [7]. Therefore, after the module is assembled, a mechanical environment test is required to investigate the internal sensitive components and single-machine response and further revise the module design and mechanical environment conditions. As the intermediate component between the vibration table and the module, the stiffness and mechanical transfer characteristics of the test platform are particularly important for the safety of mechanical tests and the accuracy of test results. Therefore, the development and design of the mechanical test platform are the basis for ensuring the normal launch of the module and subsequent scientific detection.

This paper conducts a preliminary design of the module mechanical test platform, uses finite element software to optimize the design and sensitivity analysis of the mechanical test platform, determines the final design scheme and conducts mechanical environment vibration analysis, and finally conducts mechanical environment experimental tests on the design scheme to provide a technical basis for the scientific probe module of the space telescope coronagraph.

2. Structural Features of the Test Platform

The scientific probe module has a flat structure, with three upper interfaces A, B, and C distributed on the three end faces of the module, as shown in Figure 1.

The design of the test platform needs to consider economy, module installation accessibility, platform stiffness, and interface dynamic response. The test platform is mainly divided into the platform base plate and the interface mounting brackets. In order to reduce the module installation height, the module is installed horizontally on the test platform during design. The mounting bracket at point A is an integrated machined boss structure and the mounting brackets at points B and C of the interface are assembled by screwing after plate processing, which reduces the cost of materials and machining. At the same time, considering the selection of the subsequent test vibration table, the lightweight aluminum alloy 2A12-T4 with high specific stiffness is selected as the test platform material during design to reduce the mass of the test platform and reduce the thrust index requirements of the vibration test table. The physical properties of the aluminum alloy 2A12-T4 material are shown in Table 1.

According to the structural characteristics of the scientific probe module, the test platform was preliminarily designed, and the structural diagram is shown in Figure 2. The mounting bracket at point A has good rigidity and low response amplification, so this paper mainly optimizes and analyzes the mounting bracket structure at interfaces B and C. Since the bracket is made of plate processing and splicing, the factors affecting the overall rigidity of the test platform and the module interface response are mainly the thickness and position of the back rib plate. Affected by the spatial layout, the optimization parameters are the thickness parameters of the rib plates on both sides of the mounting brackets at interfaces B and C, whose structures are shown in Figure 3. According to the design requirements, the fundamental frequency of the module mechanical test platform is 3 to 5 times the fundamental frequency of the module [8, 9]. For the mechanical test platform of the scientific probe module, its fundamental frequency needs to be greater than 300 Hz, and the vibration response value should be low.

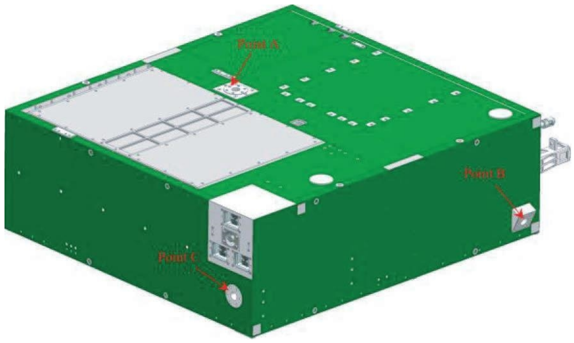

Figure 1: Structural model of the scientific probe module.

Table 1: Physical properties of 2A12-T4.

Density	Elastic modulus	Poisson's ratio
$2.8e3\,kg/m^3$	71 GPa	0.33

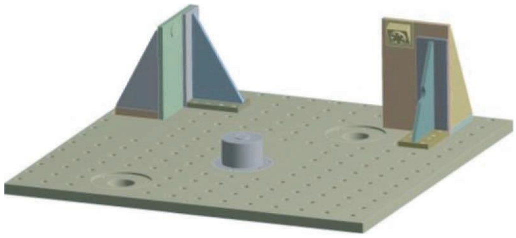

Figure 2: Schematic diagram of the mechanical test platform.

3. Modal Analysis of the Test Platform

The objective of modal analysis is to determine the product's natural frequencies and mode shapes, requiring the test platform to exhibit high stiffness with minimal response while preventing resonance between the platform and test module to ensure testing safety.

According to vibration theory and finite element modal analysis theory, the general dynamic equation of structural vibration of elastic vibration systems with multiple degrees of freedom is as follows [10, 11]:

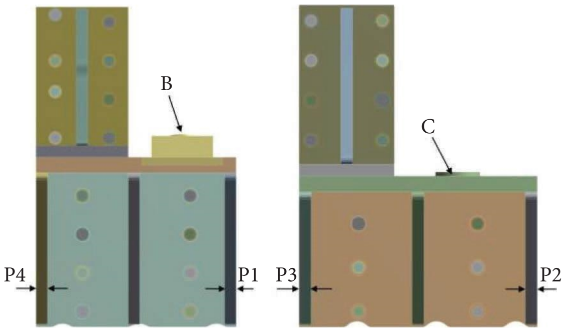

Figure 3: Parameter diagram of the BC point mounting bracket.

$$M\{\ddot{x}\} + C\{\dot{x}\} + K\{x\} = F(t), \tag{1}$$

where M is the mass matrix; C is the damping matrix; K is the stiffness matrix; $F(t)$ is the excitation force column vector; $\{\ddot{x}\}$ represents the acceleration response; $\{\dot{x}\}$ represents the velocity response; and $\{x\}$ represents the displacement response.

When solving the fundamental frequency and vibration mode of the free vibration of the metal assembly structure, the structural damping is small and has a very small impact on it, which can be ignored. Since there is no force in the modal analysis, that is, $F(t) = \{0\}$, equation (1) can be simplified to the undamped structural vibration motion equation as follows:

$$M\{\ddot{x}\} + K\{x\} = 0. \tag{2}$$

Then, its characteristic equation is

$$\left(K - \omega^2 M\right)M = \{0\}, \tag{3}$$

where ω represents the fundamental frequency of the system.

4. Optimization Design of the Test Platform Model

4.1. Experimental Design. The test platform was designed for the experiment. In order to study the influence of each rib on the result, the value ranges of the right rib thickness p_1, the left rib thickness p_4, the right rib thickness p_2, the left rib thickness p_3 of the B-interface mounting bracket, and the C-interface mounting bracket were set, as shown in Figure 3 and Table 2.

To simplify the calculation, the test platform simulation model only retains the screw connection between the B and C interface mounting brackets and the base plate. The screw size is M8, the screw preload is set to 10750N, the contact relationship is friction contact, the friction coefficient is 0.1, and the contact relationship between the remaining parts is simplified to binding contact. The central composite design method is used to design the test platform, and the fundamental frequency f and amplitude A results obtained by prestressed modal simulation are shown in Table 3. Figure 4 shows the sensitivity distribution of the four parameters.

Comprehensive model layout and test results show that $p_1 \sim p_4$ is proportional to the fundamental frequency and inversely proportional to the amplitude. When a parameter value in $p_1 \sim p_4$ is lower than a certain threshold (< 6.5 mm), the fundamental frequency presents a local mode of the single board; when it is higher than a certain threshold, the maximum change of the fundamental frequency is 4.3% and the maximum change of the amplitude is 10%, both of which are relatively low.

From the sensitivity distribution in Figure 4, it can be seen that for parameters $p1$ and $p3$, the absolute values of their contributions to the fundamental frequency and amplitude are both greater than 80%. In contrast, for $p2$ and $p4$, the absolute values of their contributions to both the fundamental frequency and amplitude are less than 70%. Additionally, the correlation between the parameters is relatively high.

4.2. Response Surface Model Establishment and Analysis. The response surface method enables multiparameter-influenced target optimization by generating response-design variable correlations through experimental data fitting. Xing et al. [12–15] analyzed heat sink structural/flow parameter effects on thermal dissipation efficiency, employing RSM to develop quadratic regression models and identify Pareto-optimal solutions that enhanced heat exchanger efficiency by 12.7%–18.3%. Wang et al. [16] conducted RSM-based analysis of gas-liquid cyclone separators, quantifying structural/operational parameter impacts on separation efficiency and pressure drop, establishing high-efficiency low-resistance separation systems. Liu et al. [17] applied RSM to space gravitational wave detection satellites' ultrastable structures, quantifying elastic modulus/support layout effects on anti-interference capability (error < 8%). Qin et al. [18] integrated CFD with RSM for G1 micromixer optimization, constructing quadratic polynomial models with parallel PSO to increase the flow rate by 13.51% and mixing efficiency by 2.45%. Ge et al. [19] utilized RSM for electric vibration table optimization, enhancing vibration uniformity/load capacity by 15.2%–22.6% through parameter interaction analysis. Zhang et al. [20] optimized high-temperature strain gauge grids via RSM, reducing measurement errors by 22.7% and temperature drift coefficients by 18.5%. Liu et al. [21, 22] implemented RSM for structural-acoustic radiation optimization, achieving 5.8–9.3 dB noise reduction. In this section, the response surface method is used to study the relationship between the stiffener wall thickness and the fundamental frequency and amplitude of the test platform. The functional relationship between the parameters is shown in the following formula.

$$\begin{aligned} y_f &= f(x), \\ y_A &= g(x), \end{aligned} \tag{4}$$

where y_f and y_A are the fundamental frequency and amplitude of the test platform, respectively.

Table 2: Value range.

Range	p_1 (mm)	p_2 (mm)	p_3 (mm)	p_4 (mm)
Minimum	2	2	2	2
Maximum	20	20	20	20

Table 3: Experimental scheme and results.

Sample points	p_1 (mm)	p_2 (mm)	p_3 (mm)	p_4 (mm)	f (Hz)	A (mm)
1	11	11	11	11	490.387	25.427
2	2	11	11	11	176.557	201.983
3	6.5	11	11	11	482.45	49.0672
4	20	11	11	11	499.335	23.297
5	15.5	11	11	11	491.588	24.409
6	11	2	11	11	248.958	240.044
7	11	6.5	11	11	490.348	25.427
8	11	20	11	11	490.387	25.427
9	11	15.5	11	11	490.388	25.427
10	11	11	2	11	176.279	201.753
11	11	11	6.5	11	483.356	51.274
12	11	11	20	11	488.078	24.945
13	11	11	15.5	11	489.011	25.227
14	11	11	11	2	250.352	240.687
15	11	11	11	6.5	490.388	25.427
16	11	11	11	20	490.387	25.427
17	11	11	11	15.5	490.394	25.425
18	2	2	2	2	176.269	200.071
19	6.5	6.5	6.5	6.5	477.724	44.087
20	20	2	2	2	176.301	201.754
21	15.5	6.5	6.5	6.5	483.978	51.355
22	2	20	2	2	176.269	200.073
23	6.5	15.5	6.5	6.5	477.721	44.086
24	20	20	2	2	176.301	201.754
25	15.5	15.5	6.5	6.5	484.291	51.668
26	2	2	20	2	176.588	201.98
27	6.5	6.5	15.5	6.5	481.56	48.348
28	20	2	20	2	248.954	239.883
29	15.5	6.5	15.5	6.5	490.116	24.229
30	2	20	20	2	176.588	201.98
31	6.5	15.5	15.5	6.5	481.526	48.327
32	20	20	20	2	250.361	240.688
33	15.5	15.5	15.5	6.5	490.118	24.229
34	2	2	2	20	176.27	200.079
35	6.5	6.5	6.5	15.5	477.723	44.087
36	20	2	2	20	176.301	201.754
37	15.5	6.5	6.5	15.5	484.314	51.688
38	2	20	2	24	176.27	200.079
39	6.5	15.5	6.5	15.5	477.718	44.085
40	20	20	2	20	176.301	201.754
41	15.5	15.5	6.5	15.5	484.292	51.669
42	2	2	20	20	176.587	201.98
43	6.5	6.5	15.5	15.5	481.523	48.32
44	20	2	20	20	248.962	240.046
45	15.5	6.5	15.5	15.5	490.149	24.229
46	2	20	20	20	176.587	201.98
47	6.5	15.5	15.5	15.5	481.552	48.342
48	20	20	20	20	496.712	22.901
49	15.5	15.5	15.5	15.5	490.149	24.229

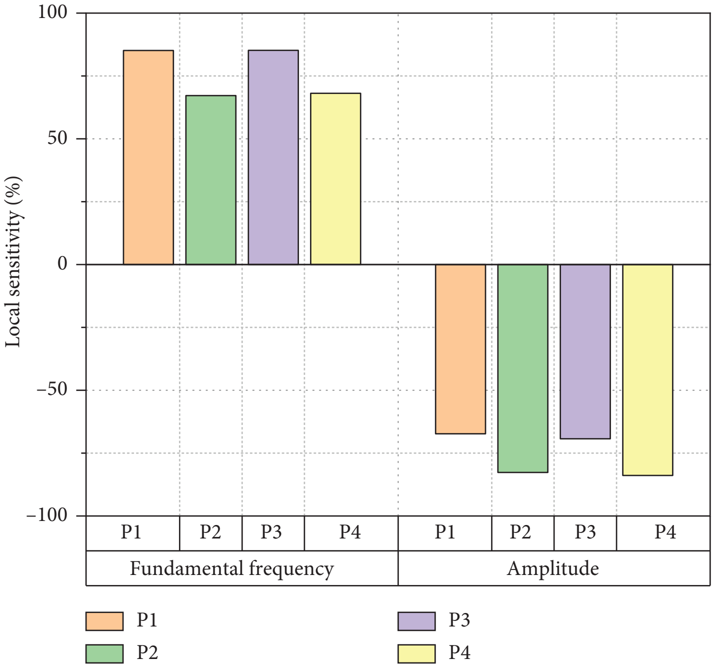

FIGURE 4: Sensitivity distribution diagram.

The actual functional relationship between the response y and the variable $x = (p_1, p_2, p_3, p_4)$ is very complex, so an approximate functional relationship is used to fit a regression equation containing a cubic term to obtain a third-order response surface model, whose expression is shown in the following formula:

$$y = \sum_{i=1}^{k} a_i x_i + \sum_{i=1}^{k} a_{iii} x_i^2 + \sum_{i=1}^{k} a_{iii} x_i^3 + \sum_{i=1,j=1}^{k} a_{ij} x_i x_j + \varepsilon. \quad (5)$$

In the formula, a represents the regression coefficient, ε is the deviation, and k is the number of variables.

In order to prove the fitting accuracy of the fitting model, it is necessary to perform error analysis on the fitting model. Therefore, the following parameters are introduced: sst is the total sum of squares, that is, the sum of squares of the difference between the test value and the average value of the test value; ssr is the regression sum of squares, that is, the sum of squares of the difference between the fitting value and the average value of the test value; and sse is the residual sum of squares, that is, the sum of squares of the difference between the test value and the fitting value [23]. The relationship between the parameters is shown in the following formula.

$$\begin{aligned} \text{sst} &= \sum_{i=1}^{n} (y_i - \overline{y})^2, \\ \text{ssr} &= \sum_{i=1}^{n} (y_a - \overline{y})^2, \\ \text{sst} &= \text{ssr} + \text{sse}. \end{aligned} \quad (6)$$

Therefore, the error determination coefficient of the fitting model is shown in the following formula.

$$\begin{aligned} r^2 &= \frac{\text{ssr}}{\text{sst}} = 1 - \frac{\text{sse}}{\text{sst}}, \\ r_{\text{adj}}^2 &= 1 - \frac{\text{sse}/(n-d)}{\text{sst}/(n-1)}. \end{aligned} \quad (7)$$

Among them, r^2 is the accuracy determination coefficient, r_{adj}^2 is the correction coefficient for removing the number of terms in the regression equation, n is the total number of experimental values, and d is the total number of terms in the fitting equation. When the fitting model accuracy is higher, r^2 is closer to 1, r^2 and r_{adj}^2 are closer to each other.

Based on the above model and the data in Table 3, the fitting is performed, and the local modal sample points with large discreteness are eliminated during the fitting, and the fundamental frequency response surface model of the test platform is obtained as follows:

$$\begin{aligned} y_f = {} & 0.0254 p_1^3 - 0.0014 p_2^3 + 0.016 p_3^3 - 0.016 p_4^3 \\ & - 0.997 p_1^2 + 0.0535 p_2^2 - 0.727 p_3^2 + 0.0607 p_4^2 \\ & - 0.00185 p_1 p_2 + 0.023 p_1 p_3 - 0.0015 p_1 p_4 \\ & - 0.0037 p_2 p_3 - 0.0037 p_2 p_4 - 0.0037 p_3 p_4 \\ & + 12.834 p_1 - 0.53 p_2 + 10.25 p_3 - 0.62 p_4 + 391.7. \end{aligned} \quad (8)$$

The accuracy determination coefficient r^2 is 0.9976, and the correction coefficient r_{adj}^2 is 0.9974. The two are almost consistent and both tend to 1. The fitting model is effective and of excellent quality.

Similarly, the amplitude response surface model of the test platform is obtained by eliminating the sample points with large discreteness as follows:

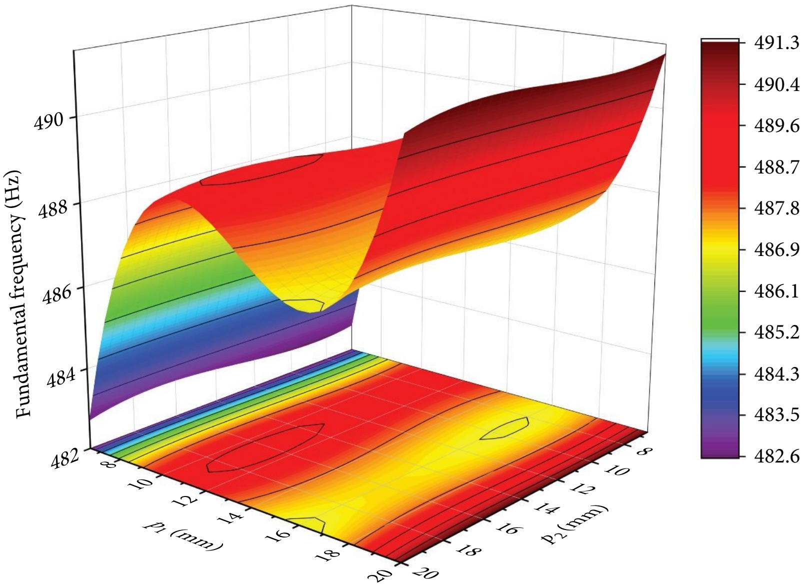

Figure 5: $p_3 = 10$ mm base frequency response surface cloud diagram.

$$y_A = -0.04p_1^3 + 0.0084p_3^3 + 1.886p_1^2 - 0.393p_3^2 - 28.62p_1 + 5.89p_3 + 137.58. \tag{9}$$

The accuracy determination coefficient r^2 is 0.9999, and the correction coefficient r_{adj}^2 is 0.9999. The two are almost consistent and both tend to 1. The fitting model is effective and of excellent quality.

Since the ABC interface of the test platform is the product installation position, when the module-level mechanical environment test is performed, p_1 and p_2 have a greater impact on the stiffness of the assembly. At the same time, it can be observed from Table 3 that the p_3 threshold is around 11 mm and the p_4 threshold is around 6.5 mm. When the actual test platform is assembled, the ribs are fastened with M6 screws. Considering the material of the test platform and the safety of disassembly and assembly, M8–M6 wire screw sleeves need to be nested on the ribs. Therefore, the final thickness of each rib should not be less than 10 mm. Based on the above results, it can be preliminarily inferred that the value of p_3 is an integer and the value of p_4 is 10 mm.

When p_3 and p_4 are both 10 mm, formula (8) can be simplified to the following formula:

$$y_{f1} = 0.0254p_1^3 - 0.0014p_2^3 - 0.997p_1^2 + 0.0535p_2^2 - 0.00185p_1p_2 + 13.049p_1 - 0.604p_2 + 435.4. \tag{10}$$

When p_3 is 11 mm and p_4 is 10 mm, formula (8) can be simplified to the following formula:

$$y_{f2} = 0.0254p_1^3 - 0.0014p_2^3 - 0.997p_1^2 + 0.0535p_2^2 - 0.00185p_1p_2 + 13.349p_1 - 0.608p_2 + 435.64. \tag{11}$$

The fundamental frequency response surface cloud diagrams of the test platform under the two design conditions are shown in Figures 5 and 6. At the same time, the output amplitude response surface cloud diagram is shown in Figure 7.

As shown in Figures 5 and 6, the fundamental frequency is slightly higher when it is 11 mm, but only 0.6% higher; since the values of each parameter are integers, this paper does not optimize the optimal value. Considering the influence of fundamental frequency, amplitude, and economy, the optimal design values of p_1 and p_2 are 12 and 10 mm, respectively. Therefore, the four parameters of the test platform are 12, 10 mm, 10, and 10 mm, respectively, and the fitting fundamental frequency and amplitude of the test platform are 489.98 Hz and 24.6 mm, respectively.

5. Dynamics Simulation Analysis

5.1. Modal Analysis. Utilizing the aforementioned parameters, the test platform structure was geometrically refined. An automatic meshing scheme employing SOLID186 and SOLID187 elements generated 897,131 elements and 1,846,900 nodes (average mesh quality: 0.829) as shown in Figure 8. Subsequently, a prestressed modal analysis was performed under the boundary conditions defined in Section 2 (including a fully fixed constraint on the baseplate's

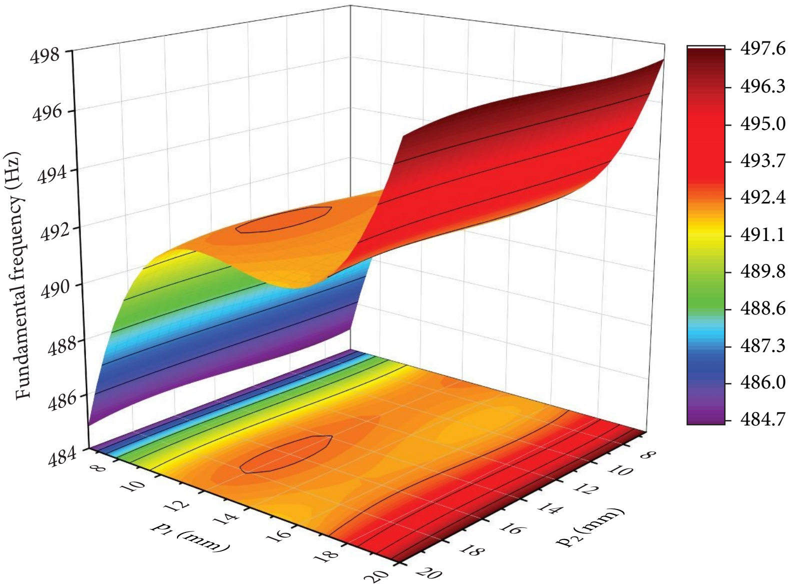

Figure 6: $p_3 = 11$ mm fundamental frequency response surface cloud diagram.

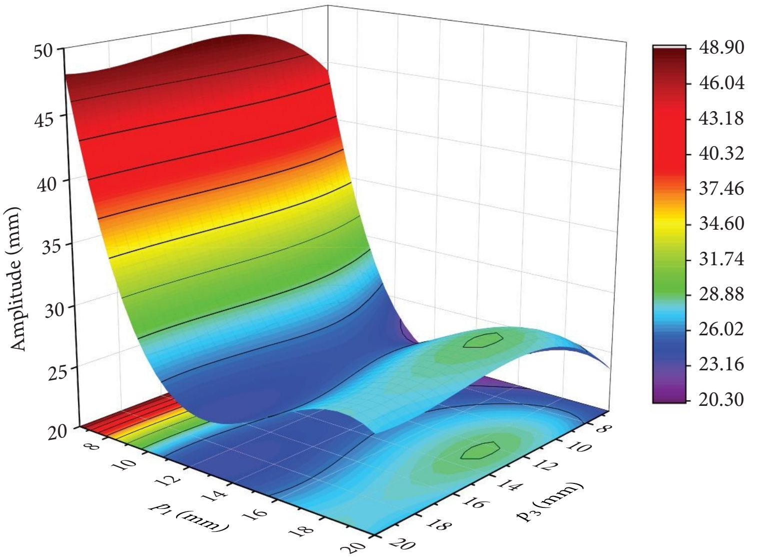

Figure 7: Amplitude response surface cloud diagram.

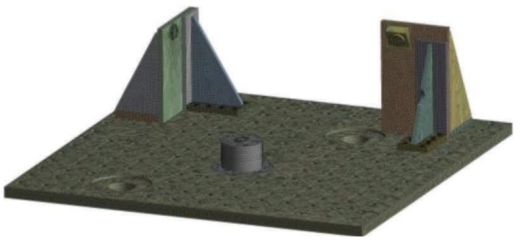

Figure 8: Grid model.

inferior surface) extracted the first 32 structural modes, with the mode shapes of the first to sixth orders shown in Figures 9, 10, 11, 12, 13, and 14.

As can be seen from the results in Table 4, the first- to sixth-order natural frequencies of the test platform are 472.88, 638.2, 804.85, 940.9, 981.05, and 1025.2 Hz, respectively. Due to model refinement, minor discrepancies exist between the fundamental frequency, amplitudes, and the fitting results. The mass fractions for each mode in

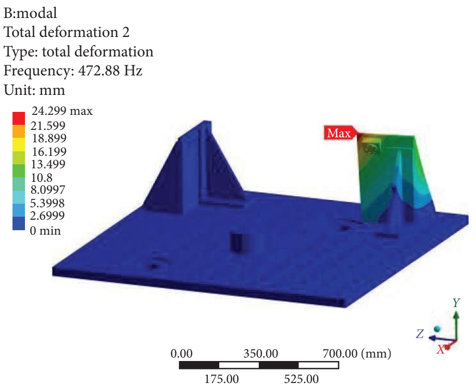

Figure 9: First-order vibration mode.

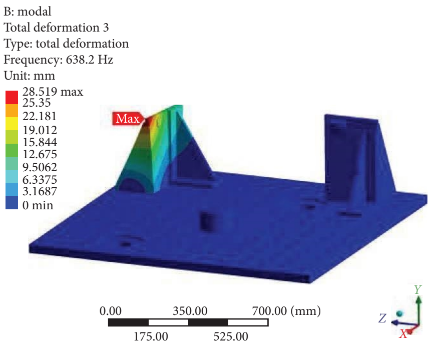

Figure 10: Second-order vibration mode.

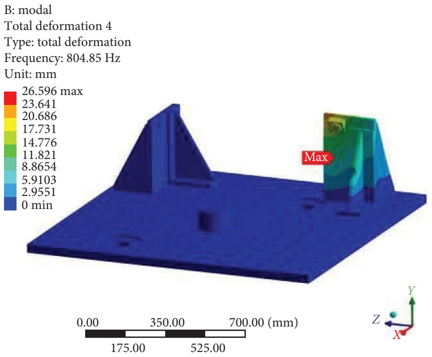

Figure 11: Third-order vibration mode.

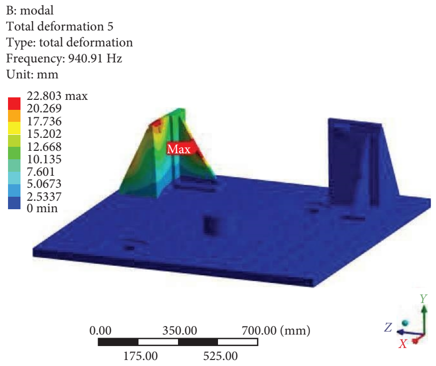

Figure 12: Fourth-order vibration mode.

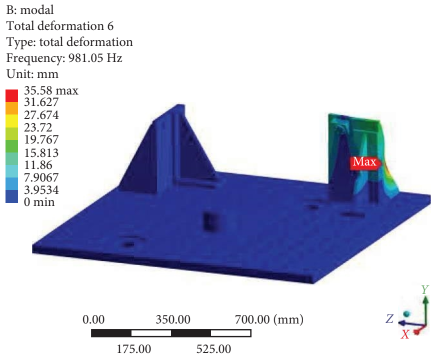

Figure 13: Fifth-order vibration mode.

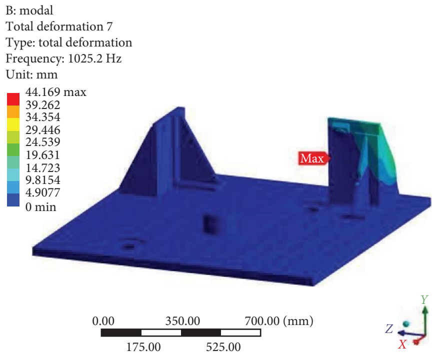

Figure 14: Sixth-order vibration mode.

various directions are presented in Table 4. Based on the mass fractions, the mode shapes primarily involve translational motion of the part along the X and Z directions, rotation about the Y direction, and coupled vibrations in these directions. The amplitudes in all other directions are negligible.

5.2. Vibration Simulation Analysis. In order to ensure the structural safety of the coronagraph scientific probe module during the dynamic test, it is necessary to simulate and analyze the dynamic characteristics of the test platform. The sinusoidal and random vibration test conditions are shown in Tables 5 and 6.

Based on the aforementioned vibration conditions, simulation analysis was performed on the test platform, with the structural damping coefficient referenced from Section 5. The maximum stress of the sinusoidal vibration response was 1.75 MPa in the Z direction; for the random vibration response, the calculated 3σ peak stress level in the Z direction was 26.485 MPa, obtained using modal

Table 4: Comparison of results.

Order	***f* (Hz)**	**Mass fraction (%)**					
		X	***Y***	***Z***	**RX**	**RY**	**RZ**
First	472.88	0.595	0.049	2.41	0.037	1.37	0.033
Second	638.2	1.69	0.025	0.794	0.04	1.8	0.007
Third	804.85	2.23	0.013	1.57	0.007	0.024	0.08
Fourth	940.9	0.462	0.014	0.692	0.023	4.6	0.012
Fifth	981.05	0.808	0.021	0.199	0.006	0.024	0.059
Sixth	1025.2	0.106	0	0.024	0	0.015	0.008

Table 5: Sinusoidal vibration test conditions.

***X* direction (sweep rate: 2 oct/min)**				
f (Hz)	5~10	10~14	14~75	75~100
A	7.45 mm	3 g	5.5 g	4 g
***Y*, *Z* direction (sweep rate: 2 oct/min)**				
f (Hz)	5~10	10~14	14~70	70~100
A	9.93 mm	4 g	7 g	4 g

Table 6: Random vibrations test conditions.

X, Y, *Z* direction		
PSD	20~100 Hz	3 dB/oct
	100~600 Hz	0.02 g^2/Hz
	600~2000 Hz	−9 dB/oct
RMS	4.02 g	
Duration	3 min	

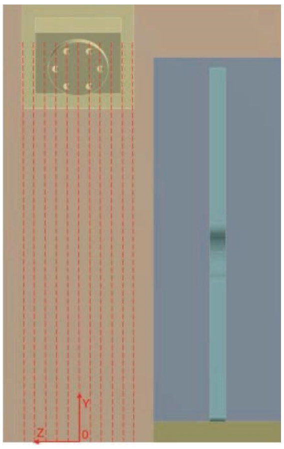

Figure 15: B point mounting path diagram.

Figure 16: Test platform frequency sweep test.

superposition-based analysis with the input PSD excitations. The test platform is made of 2A12-T4 aluminum alloy, whose allowable stress is 210 MPa. Based on this 3σ random stress level, the minimum safety factor of the test platform is 7.93, which is greater than the structural component yield limit safety factor of 1.2 and the failure load safety factor of 1.35 required by aerospace [24]. Therefore, the test platform meets the structural safety design requirements.

The test platform was simulated by sweeping the frequency in three directions in the range of 0~500 Hz with an input of 0.2 g, and the acceleration response of the test platform under the fundamental frequency condition was obtained. Among them, the test platform is insensitive to *Y* direction excitation, so only the acceleration response curves of the path of B point (the center of B point is connected with the bottom, see Figure 15 for details) and the paths near the *Z* direction at the fundamental frequency in the *X* and *Z* directions are output as shown in the following.

From the fundamental frequency vibration mode and the path response diagram, it is evident that resonant responses occur in both the *X* and *Z* directions at the fundamental frequency, with the response in the *Z* direction being slightly higher. The curve exhibits a steeper gradient along the path from the bottom of the mounting base to the center height of mounting B point. When sweeping in the *X* direction the acceleration response at the center height of mounting B point is amplified by approximately 25.8 times, and the acceleration response in the *Z* direction is amplified by approximately 53.4 times. Concurrently, the average response increment per 10 mm interval is approximately 0.44 g. Each curve, spanning a distance of 100 mm–360 mm from the bottom of the mounting base to the center of mounting B point, is essentially linear. Therefore, if further response optimization is undertaken in the future, incorporating transverse ribs between the central and right rib

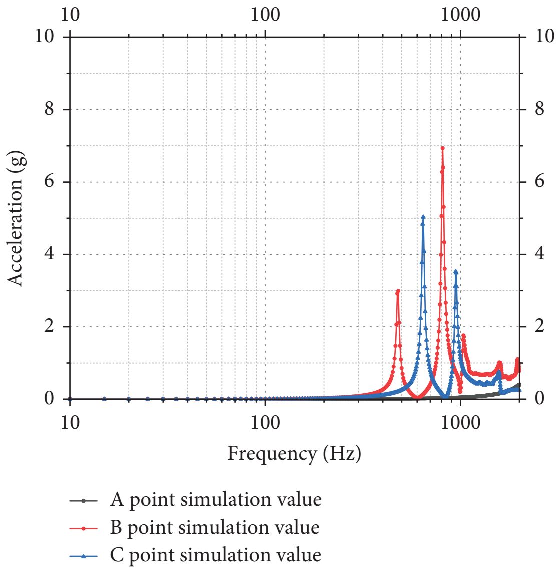

Figure 17: *X* direction acceleration simulation curve.

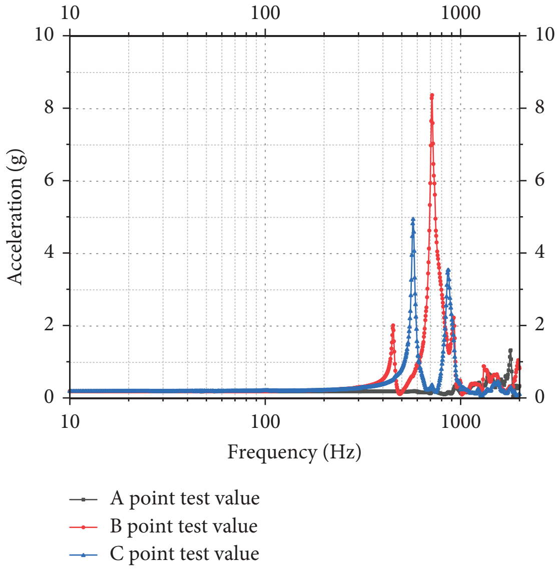

Figure 18: *X* direction acceleration test curve.

plates of mounting base B can be designed to reduce the response at the interface.

6. Experimental Verification

To verify the accuracy of the fitting and simulation results, the test platform was mounted on an 18-ton vibration table for 0.2-g sinusoidal sweep testing across 10–2000 Hz in three orthogonal directions (Figure 16). Accelerometer-monitoring points were installed near interfaces A, B, and C to record response data. The response curves of the 0.2-g sweep frequency simulation and experimental tests are shown in Figures 17, 18, 19, 20, 21, and 22.

Given the minimal modal coupling in resonance peaks and the platform's straightforward configuration, the half-power bandwidth method was employed to extract structural damping ratios from experimental curves. For simulations, damping values in the *X* and *Z* directions were set to 0.014 and 0.011, respectively, aligning with experimental measurements. The irregular *Y* direction experimental curves precluded precise damping evaluation; thus, the simulated structural damping for this direction was assigned

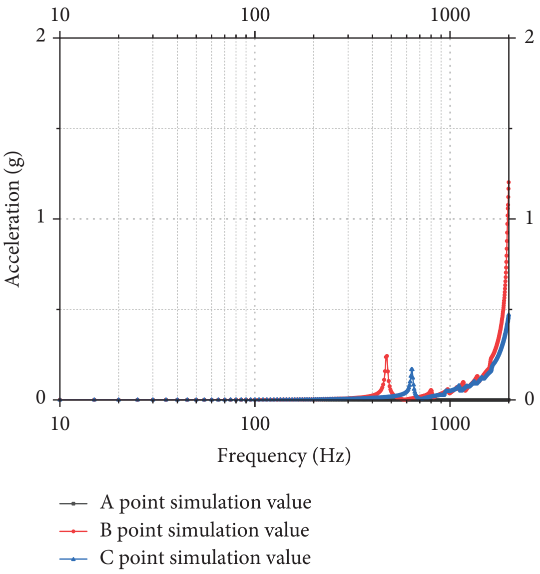

Figure 19: *Y* direction acceleration simulation curve.

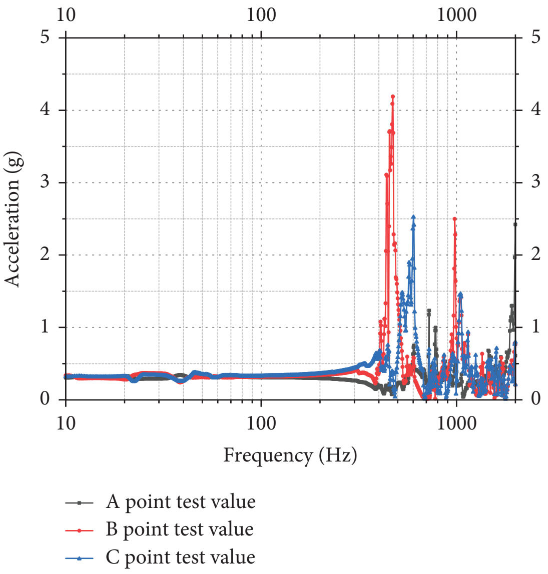

Figure 20: *Y* direction acceleration test curve.

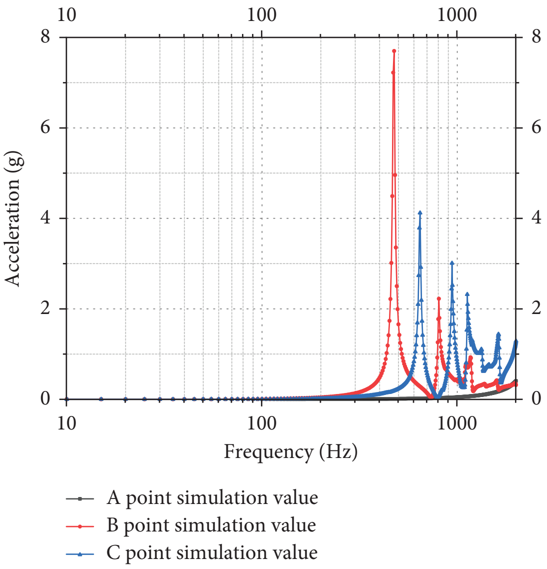

Figure 21: *Z* direction acceleration simulation curve.

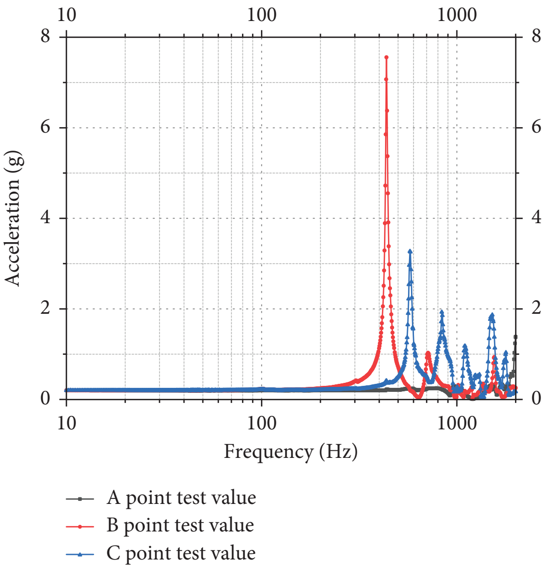

Figure 22: *Z* direction acceleration test curve.

0.012 based on comprehensive analysis of other directional data and partial *Y* direction resonance peaks.

From the analysis of the curve results, it can be seen that the resonant frequencies of the test platform in the *X* direction are 450, 571, 715, and 865 Hz; the resonant frequencies in the *Y* direction are 474, 604, 984, and 1053 Hz; and the resonant frequencies in the *Z* direction are 436.2, 577, and 837 Hz, which are compared with the simulation results as shown in Table 7. The first-order, fifth-order, and sixth-order results have good consistency, while the second-order to fourth-order results have certain divergences.

Experimental and simulated curves exhibit substantial agreement along the *X* and *Z* directions, with only minor deviations observed in select resonance peak magnitudes, thereby validating the simulation's effectiveness. However, *Y*-direction experimental curves exhibit significant anomalies and substantial divergence from simulation results. Theoretically, modal shapes, effective mass participation, and structural configuration indicate that the *Y* direction possesses the highest stiffness among all three orthogonal directions. Consequently, prominent resonance peaks should not manifest in lower-order modes. The possible reasons for the divergence are as follows:

1. Simulation condition: the simulation only considered the bolted connection and fastening relationship between Mounts B and C and the platform base plate.

Table 7: Comparison of results.

Order	Simulation results	Test results	Average error (%)
First	472.88	436.2/450/474	4.2
Second	638.2	571/577/604	8.5
Third	804.85	715	11.1
Fourth	940.9	837/865	9.5
Fifth	981.05	984	0.3
Sixth	1025.2	1053	0.07
	Average total error		5.6

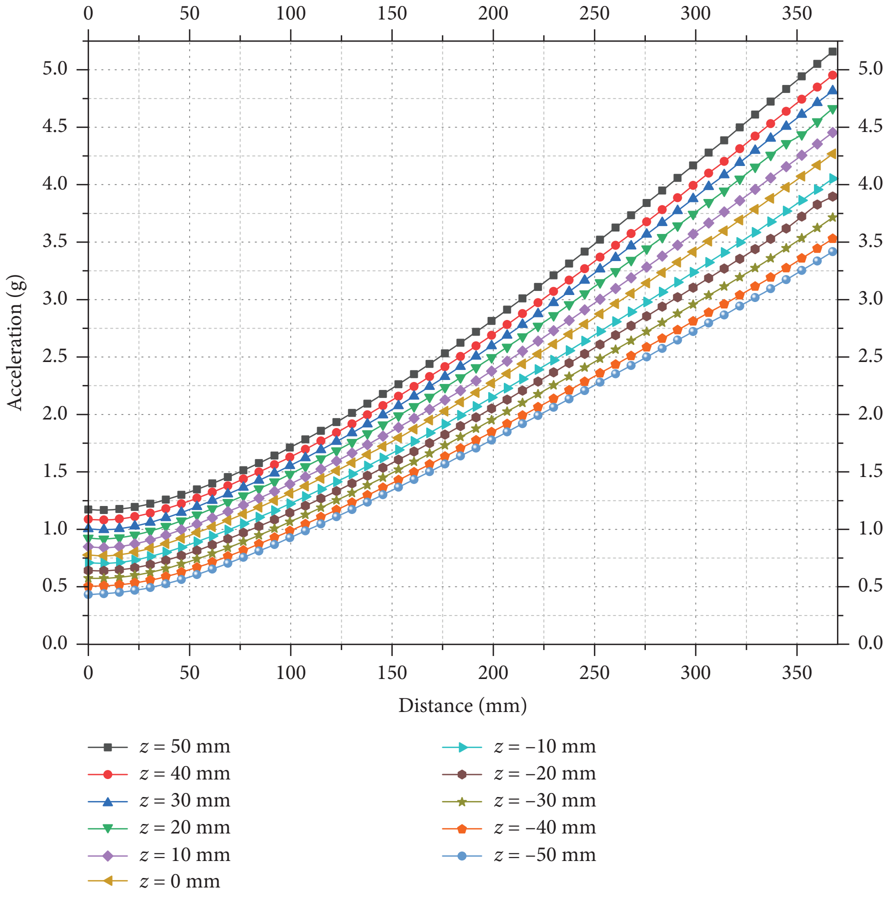

Figure 23: Acceleration response curve of X direction.

The bolted connections between the platform base plate and the test bench, as well as the mount plates, were neglected. In addition, subject to site constraints, only partial fastening screws were installed between the platform base plate and the test bench. During Y direction vibration, the vibration may cause preload loss in the fastening screws. This may be the main reason for the discrepancy between the experimental and simulation curves in the Y direction;

2. Data acquisition: as shown in Figures 23 and 24, the vibration response varies across different locations. The inconsistency between the positions of acceleration measurement points and simulation sampling nodes may result in discrepancies in acceleration amplitude. In addition, the experimental curves were sampled at a variable rate, whereas the simulation curves maintained a fixed sampling frequency, which may also cause differences in the results.

Combining the above analysis results, the actual fundamental frequency of the test platform is 436.2 Hz, which meets the design value > 300 Hz indicator requirement, and leaves a certain design margin to meet the mechanical

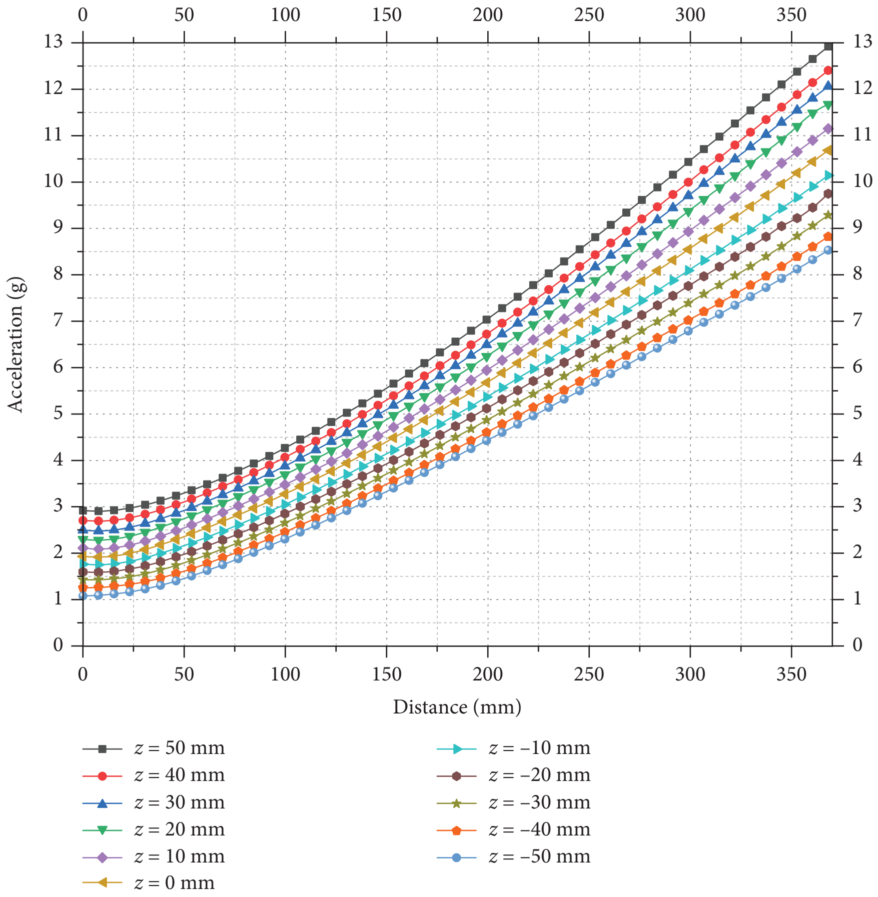

FIGURE 24: Acceleration response curve of Z direction.

environment test needs of the coronagraph scientific probe module.

7. Conclusion

The research object of this paper is the mechanical test platform of the scientific probe module of the CPI-C. According to the module layout requirements and stiffness requirements, the test platform is optimized by the response surface design. The fundamental frequency and amplitude response surface model are obtained by least squares fitting, and the final configuration parameters of the test platform are determined. The effectiveness of the optimization model is verified by dynamic simulation and sine frequency sweep test. The fundamental frequency of the test platform is 436.2 Hz, which meets the mechanical test requirements of the scientific probe module of the CPI-C at all stages. At the same time, this design method can guide the structural design of the CPI-C and provide a theoretical basis for the implementation of the Chinese space station project.

Data Availability Statement

The data that support the findings of this study are available from the corresponding author upon reasonable request.

Conflicts of Interest

The authors declare no conflicts of interest.

Funding

This research was supported by the National Natural Science Foundation of China (grant nos. 11827804, U2031210, and 12103073) and the China Manned Space Project (grant nos. CMS-CSST-2025-A18, CMS-CSST-2021-A11, CMS-CSST-2021-B04, and CMS-CSST-201906), and the pre-research project on Civil Aerospace Technologies No. D010301 funded by China National Space Administration (CNSA).

Acknowledgments

This research was supported by the National Natural Science Foundation of China (grant nos. 11827804, U2031210, and 12103073) and the China Manned Space Project (grant nos. CMS-CSST-2025-A18, CMS-CSST-2021-A11, CMS-CSST-2021-B04, and CMS-CSST-201906), and the pre-research project on Civil Aerospace Technologies No. D010301 funded by China National Space Administration (CNSA).

References

[1] H. Zhan, "Introduction for Chinese Survey Space Telescope," *China Astronomical Conference Paper* (2021).

[2] M. Xu, W. Guo, and L. Kong, "Optimization Design and Analysis for the Optics Bench Structure of the Cool Planet Imaging Coronagraph Module," *Spacecraft Environment Engineering* (2023).

[3] D. Ren and Y. Chen, "Global Optimization-based Reference Star Differential Imaging for High-Contrast Exoplanet Imaging Survey," *Monthly Notices of the Royal Astronomical Society* 502, no. 2 (2021): 2158–2171, https://doi.org/10.1093/mnras/stab022.

[4] Y. Zhu, J. Dou, X. Zhang, G. Zhao, J. Guo, and L. Infante, "Portable Adaptive Optics for Exoplanet Imaging," *Research in Astronomy and Astrophysics* 21, no. 4 (2021): 082, https://doi.org/10.1088/1674-4527/21/4/82.

[5] J. Dou, Y. Zhu, and D. Ren, "Current Research Status of Exoplanets," *Chinese Journal of Nature* (2014).

[6] J. Dou and D. Ren, "Phase Quantization Study of Spatial Light Modulator for Extreme High-Contrast Imagining," *The Astrophysical Journal* 832, no. 1 (2016): 84, https://doi.org/10.3847/0004-637x/832/1/84.

[7] Y. Yan and J. Yao, "Design and Analysis of Dynamic Characteristics of the Optical Satellite Vibration Fixture," *Infrared and Laser Engineering* (2014).

[8] C. An, H. Zhao, Z. Zhang, and L. Ge, *Design and Analysis of Vibration Tong for EO Equipments* (Electro-Optic Technology Application, 2004).

[9] W. Li, *Design and Research of Vibration Tong for Space Optical Remote Sensor* (OEM Information, 2010).

[10] X. Tao, M. Ahmat, G. Sun, and W. Zhang, "Random Vibration Response and Optimization Analysis on Welded Metal Bellows of Mechanical Sealing," *Lubrication Engineering* (2021).

[11] Y. Wu, *Fatigue Life and Analysis of Welled Metal Bellows of Mechanical Seal [D]* (Lanzhou: Lanzhou University of Technology, 2017).

[12] J. Xing, S. Han, and T. Huo, "Flow and Heat Transfer Characteristics of bio-inspired rhombus-patterned Ribs: Performance Optimization Using Response Surface Methodology," *International Journal of Thermal Sciences* 199 (2024): 108928, https://doi.org/10.1016/j.ijthermalsci.2024.108928.

[13] B. Ma, R. Hu, Y. Wang, and Y. Cheng, "A Study on the Optimization of Cooling Performance for Oil-Immersed Transformers in High Temperature Environments Utilizing Response Surface Methodology," *Case Studies in Thermal Engineering* 63 (2024): 105353, https://doi.org/10.1016/j.csite.2024.105353.

[14] J. Zhang, X. Song, and J. Lei, "Performance and Regression Analysis of Air-Cooled Thermoelectric Cooling System Using Response Surface Methodology and Numerical Simulation," *International Journal of Heat and Mass Transfer* 228 (2024): 125617, https://doi.org/10.1016/j.ijheatmasstransfer.2024.125617.

[15] Z. Yang, W. Lu, J. Yao, Y. Cheng, D. Wu, and H. Wen, "Liquid-Cooled Plate Cooling Channels Design Based on Variable Density Topology Optimization," *Energy Storage Science and Technology* (2025).

[16] S. Wang, M. Jiang, S. Zhang, S. Yu, M. Lu, and L. Zhao, "Multi-Objective Optimization of a Novel gas-liquid Cylindrical Cyclone Based on Response Surface Methodology," *Chemical Engineering Research and Design* 212 (2024): 1–13, https://doi.org/10.1016/j.cherd.2024.10.030.

[17] C. Liu, Z. Xu, K. Han, C. Han, and T. He, "Optimization Design of Core Ultra-Stable Structure for Space Gravitational Wave Detection Satellite Based on Response Surface Methodology," *Aerospace* 11, no. 7 (2024): 518, https://doi.org/10.3390/aerospace11070518.

[18] L. Qin, X. Lu, and L. Li, "Optimization of G1 Micromixer Structure in Two-Fluid Mixing Based on CFD and Response Surface Methodology," *Processes* 12, no. 1 (2024): 122, https://doi.org/10.3390/pr12010122.

[19] P. Ge, J. Zhu, P. Yang, L. Zhang, and J. Zheng, "Optimization of Vertical Expansion Table of Electric Vibration Table Based on Response Surface Method," *Engineering & Test* (2024).

[20] F. Zhang, X. Zhang, Y. Ai, and Y. Zhao, "Sensitive Grid Structure Optimization of High Temperature Strain Gauge Based on Response Surface Methodology," *Chinese Journal of Scientific Instrument* (2023).

[21] L. Liu, J. Qin, X. Lei, Q. Liu, and R. Song, "A Study on Optimization of the structure-borne Noise from a Trough Girder Based on Response Surface Methodology," *Journal of Vibration and Shock* (2018).

[22] X. Zang, *The Optimization Design of Structural Acoustic Performance Based on Mode Shapes and Response Surface Method* (Hunan University, 2011).

[23] C. Zhu and S. Duan, "Optimal Design of Composite Panel Structure Noise Using Response Surface Method," *Noise and Vibration Control* (2023).

[24] Technology and Engineering Center for Space Utilization and Chinese Academy of Sciences, *Z/K-E0.1-04-2014 Specification for the Product Design and Construction of the Space Application System 4th Part: Structure* (Standards Press of China, 2015).